



## RESEARCH ARTICLE

10.1029/2024JH000264

## RocMLMs: Predicting Rock Properties Through Machine Learning Models

## Key Points:

- RocMLMs predict rock properties up to  $10^1$ – $10^3$  faster than commonly used methods
- RocMLMs trained with Neural Networks are more efficient compared to other regression algorithms
- RocMLM training data show good agreement with PREM and STW105 for an average mantle geotherm

## Supporting Information:

Supporting Information may be found in the online version of this article.

## Correspondence to:

B. Kerswell,  
buchanan.kerswell@umontpellier.fr

## Citation:

Kerswell, B., Cerpa, N. G., Tommasi, A., Godard, M., & Padrón-Navarta, J. A. (2024). RocMLMs: Predicting rock properties through machine learning models. *Journal of Geophysical Research: Machine Learning and Computation*, 1, e2024JH000264. <https://doi.org/10.1029/2024JH000264>

Received 29 APR 2024

Accepted 1 AUG 2024

Buchanan Kerswell<sup>1</sup> , Nestor G. Cerpa<sup>1</sup> , Andréa Tommasi<sup>1</sup> , Marguerite Godard<sup>1</sup> , and José Alberto Padrón-Navarta<sup>2</sup>

<sup>1</sup>Geosciences Montpellier, University of Montpellier, CNRS, University of Antilles, Montpellier, France, <sup>2</sup>Instituto Andaluz de Ciencias de la Tierra (IACT), CSIC, Armilla (Granada), Spain

**Abstract** Mineral phase transformations significantly alter the bulk density and elastic properties of mantle rocks and consequently have profound effects on mantle dynamics and seismic wave propagation. These changes in the physical properties of mantle rocks result from evolution in the equilibrium mineralogical composition, which can be predicted by the minimization of the Gibbs Free Energy with respect to pressure (P), temperature (T), and chemical composition (X). Thus, numerical models that simulate mantle convection and/or probe the elastic structure of the Earth's mantle must account for varying mineralogical compositions to be self-consistent. Yet coupling Gibbs Free Energy minimization (GFEM) approaches with numerical geodynamic models is currently intractable for high-resolution simulations because prediction speeds of widely-used GFEM programs ( $10^0$ – $10^2$  ms) are impractical in many cases. As an alternative, this study introduces machine learning models (RocMLMs) that have been trained to predict thermodynamically self-consistent rock properties at arbitrary PTX conditions between 1–28 GPa and 773–2,273 K, and dry mantle compositions ranging from fertile (Iherzolitic) to refractory (harzburgitic) end-members defined with a large data set of published mantle compositions. RocMLMs are  $10^1$ – $10^3$  times faster than GFEM calculations or GFEM-based look-up table approaches with equivalent accuracy. Depth profiles of RocMLMs predictions are nearly indistinguishable from reference models PREM and STW105, demonstrating good agreement between thermodynamic-based predictions of density,  $V_p$ , and  $V_s$  and geophysical observations. RocMLMs are therefore capable, for the first time, of emulating dynamic evolution of density,  $V_p$ , and  $V_s$  due to partial melting and refertilization of dry mantle rocks in high-resolution numerical geodynamic models.

**Plain Language Summary** The mineralogical makeup of rocks within Earth's mantle largely determines how the mantle flows over geologic time, and how it responds to seismic waves triggered by earthquakes, because mineral assemblages control important rock properties such as density and stiffness (elasticity). The mineralogy of mantle rocks is not constant, however. It changes depending on three factors: pressure, temperature, and the chemical composition of the rock. Thus, it is important for computer simulations of mantle convection to account for the evolution of rock mineralogy. Computer programs that can predict rock properties based on thermodynamic calculations are available, but are generally too slow to be used in high-resolution simulations. As an alternative approach, this study introduces machine learning models (RocMLMs) that have “learned” how to predict rock properties (density and elasticity) by “training” on a large data set of thermodynamic calculations. We demonstrate that RocMLMs can then predict rock properties up to  $10^1$ – $10^3$  times faster than state-of-the-art methods. We tested RocMLM predictions against reference mantle models based on observations of seismic waves and found good agreement. RocMLMs are therefore capable of fast and highly-accurate predictions of changes in rock properties and can be implemented in high-resolution computer simulations of mantle convection.

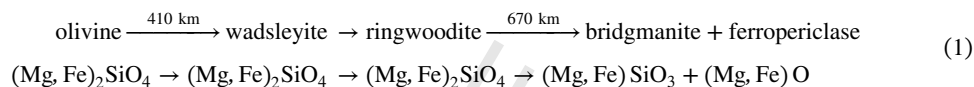
## 1. Introduction

The dominant mineral phases in Earth's mantle are olivine, pyroxene, garnet, wadsleyite, ringwoodite, bridgmanite, ferropericlase, calcium silicate perovskite, and  $\text{MgSiO}_3$  post-perovskite (e.g., Stixrude & Lithgow-Bertelloni, 2012). Mantle mineralogy evolves with depth by a series of relatively discontinuous phase transformations that define sharp transitions in the physical properties of mantle rocks (Ringwood, 1991). The most important phase transformations occur at depths between 410 and 670 km beneath Earth's surface, defining the transition from the upper to the lower mantle (Equation 1). This mantle transition zone (MTZ) is characterized by sharp variations in density and elastic properties that strongly impact mantle convection (Christensen, 1995;

© 2024 The Author(s). Journal of Geophysical Research: Machine Learning and Computation published by Wiley Periodicals LLC on behalf of American Geophysical Union.

This is an open access article under the terms of the Creative Commons Attribution License, which permits use, distribution and reproduction in any medium, provided the original work is properly cited.

Fukao et al., 2001; Jenkins et al., 2016; Karato et al., 2001; Kuritani et al., 2019; Nakagawa & Buffett, 2005; Ringwood, 1991; Schubert et al., 1975; Tackley et al., 1994; Wang et al., 2015), and the propagation of teleseismic waves (Dziewoński & Anderson, 1981; Ita & Stixrude, 1992; Ringwood, 1991). The MTZ is therefore an essential feature for modeling mantle structure and dynamics. With respect to a simple FeO-MgO-SiO<sub>2</sub> chemical system, the most important MTZ reactions can be written as:



These phase changes (e.g., Equation 1) are often parameterized in numerical geodynamic simulations with simple pressure-temperature (PT)-dependent reaction boundaries based on high-pressure experiments (e.g., Agrusta et al., 2017; Ballmer et al., 2015; Christensen, 1995; Čížková & Bina, 2013; Kerswell et al., 2021; Liu et al., 1991; Nakagawa & Buffett, 2005; Tackley et al., 1994; Torii & Yoshioka, 2007). Alternatively, some numerical geodynamic experiments (e.g., Li et al., 2019; Yang & Faccenda, 2020) use Gibbs Free Energy minimization (GFEM) programs (e.g., Connolly, 2009; Riel et al., 2022) to precompute Lookup Tables of rock properties, which are subsequently referenced to adjust material properties as the numerical experiments evolve. These implementations usually consider fixed ideal mantle compositions, such as pyrolite, and/or approximate phase transitions with simple functions. These approaches neglect the PT dependency of mineral transitions on natural variations of mantle composition (X) such as variations of Fe-Mg and Al-Ca that may be either primordial or result from melt extraction or refertilization reactions during melt transport. Despite these simplifications, these models have corroborated that the MTZ is a critical feature impacting subduction dynamics, mantle plume dynamics, and water cycling in the deep Earth.

More self-consistent numerical models of mantle convection would track changes in physical properties of mantle rocks by computing GFEM as a function of the evolution of PTX conditions. However, this is currently intractable for high-resolution geodynamic models because GFEM programs remain too slow ( $\geq 4\text{--}228$  ms per PTX point) to be applied recursively during a geodynamic simulation (see Supporting Information S1). Parallelization of GFEM programs can increase prediction speed by scaling the number of parallel processes (Riel et al., 2022), but continuously computing phase relations during geodynamic simulations would require GFEM prediction speed on the order of  $\leq 10^0\text{--}10^{-1}$  ms to be feasible (see Supporting Information S1), which may be difficult to achieve solely by parallelization and/or direct improvements to the current GFEM paradigm.

Here, we propose an alternative approach to predicting rock properties based on the use of machine learning models (referred to as RocMLMs) that have been “trained” on a multidimensional data set of precomputed rock properties using classical (k-Neighbors [KN], Decision Trees) and deep (Neural Network) regression algorithms. These later regression algorithms compress large amounts of thermodynamic information into highly efficient nonlinear functions, allowing RocMLMs to infer (predict) rock properties across arbitrary PTX conditions faster than any current GFEM algorithm. We demonstrate that RocMLMs are thus highly efficient emulators of GFEM programs and are well-suited for predicting bulk rock properties in numerical geodynamic models.

This article begins by detailing our method for building, training, and evaluating RocMLMs. We then demonstrate that RocMLMs can predict densities and seismic velocities in a dry upper mantle up to  $10^1\text{--}10^3$  times faster than commonly used GFEM programs with equivalent accuracies. Finally, we compare RocMLM predictions with reference models derived from seismological data sets (Dziewoński & Anderson, 1981; Kustowski et al., 2008) and discuss the accuracy and performance of RocMLMs with respect to their future implementation in numerical geodynamic models.

## 2. Methods

The following sections describe the methodologies employed in constructing, training, and assessing RocMLMs, with a focus on four primary objectives. First, define the size and scope of RocMLM training data to ensure widespread applicability of RocMLMs to the upper mantle and transition zone (Section 2.1). Second, define a generalized approach for generating RocMLM training data to ensure applicability to any GFEM program (e.g., MAgEMin, Perple\_X, and others, Section 2.2). Third, train RocMLMs on a set of input features that can be routinely computed during geodynamic simulations to ensure widespread applicability of RocMLMs to various

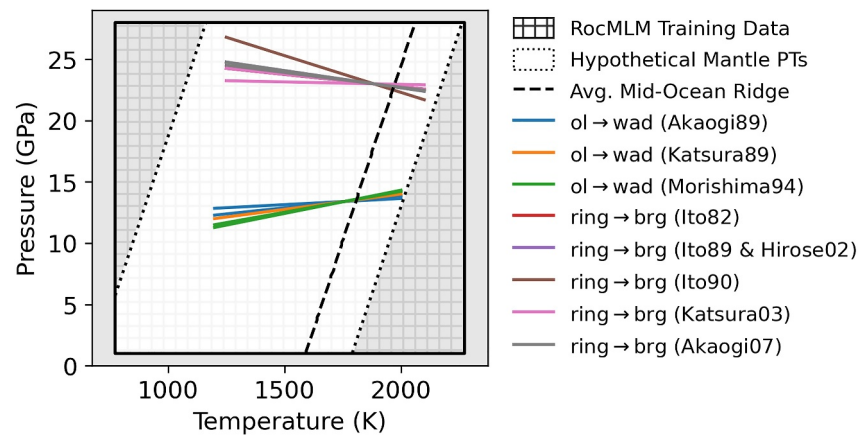


**Figure 1.** Pressure-temperature (PT) diagram showing the range of conditions considered for generating RocMLM training data (hatched region) compared to a range of possible upper mantle conditions (inner white region). The dotted black lines are geotherms with arbitrary mantle potential temperatures of 673 and 1,773 K and a constant adiabatic gradient of 0.5 K/km, representing hypothetical lower and upper bounds for mantle PT conditions (including hypothetical cold lithospheric slabs). The dashed black line is an average geotherm for a mid-ocean ridge (1,573 K adiabat). Phase boundaries for the 410 and 670 km discontinuities (colored lines) are from a compilation by Li et al. (2019).

geodynamic codes (Section 2.3). Fourth, rank the overall performance of RocMLMs in terms of accuracy and efficiency (Section 2.4).

## 2.1. RocMLM Training Data Set Design

### 2.1.1. Pressure-Temperature Conditions

High-pressure experiments constrain the reaction olivine  $\rightarrow$  wadsleyite between  $14.0 \pm 1.0$  GPa and  $1,600 \pm 400$  K with Clapeyron slopes between  $2.4 \times 10^{-3} \pm 1.4 \times 10^{-3}$  GPa/K (Akaogi et al., 1989; Katsura & Ito, 1989; Li et al., 2019; Morishima et al., 1994). Likewise, the reaction ringwoodite  $\rightarrow$  bridgmanite + ferropericlase is constrained between  $24.0 \pm 1.5$  GPa and  $1,600 \pm 400$  K with negative Clapeyron slopes between  $-2.0 \times 10^{-3} \pm 1.6 \times 10^{-3}$  GPa/K (Akaogi et al., 2007; Bina & Helffrich, 1994; Hirose, 2002; Ishii et al., 2018; Ito, 1982; Ito & Katsura, 1989; Ito & Takahashi, 1989; Ito et al., 1990; Katsura et al., 2003; Litasov et al., 2005). We therefore compute RocMLM training data within a rectangular PT region bounded between 1–28 GPa and 773–2,273 K to encompass expected conditions for the entire upper mantle and MTZ—from approximately 30 to 865 km depth (Figure 1). The machine learning models developed here are not intended to be used for predictions outside of this PT range and are therefore validated/tested within these PT conditions.

Figure 1 shows that our training data set PT range includes PT conditions that are not expected to exist in neither the Earth's mantle, nor geodynamic simulations (e.g., very cold conditions with thermal gradients  $\leq 5$  K/km, Cerpa et al., 2022; Maruyama et al., 1996; Syracuse et al., 2010). Such a large rectangular PT range might be considered impractical with respect to training efficiency (unnecessary amounts of training data) and accuracy (outside the bounds of calibrated thermodynamic data) compared to an irregular PT range bounded between arbitrary geotherms. However, initial sensitivity tests showed comparable RocMLM performance irrespective of the range of PT conditions used to generate RocMLM training data. Thus, we adopted a regular rectangular training data set design because it is computationally convenient and does not deteriorate RocMLM accuracy.

### 2.1.2. Bulk Mantle Compositions

We derived an array of synthetic dry bulk mantle compositions with the aim of encompassing the widest range of chemical variability in Earth's mantle. For this, we applied a statistical analysis to publicly-available geochemical data from thousands of natural peridotite samples. The procedure was as follows.

Bulk chemical analyses of peridotite samples were downloaded using the Earthchem.org Search Portal with a single search criterion: “set sample type > igneous rocks > names from Earthchem categories > igneous-

**Table 1**  
Summary of the Filtered and Standardized Peridotite Data Set From *Earthchem.org*

Oxide	Measured	Missing	Min*	Max*	Mean*	Median*	Std*	IQR*
SiO <sub>2</sub>	3,111	0	36.7	52	44.1	44.1	1.16	1.24
TiO <sub>2</sub>	2,835	276	0	0.268	0.051	0.03	0.05	0.068
Al <sub>2</sub> O <sub>3</sub>	3,111	0	0.023	4.95	1.65	1.31	1.14	1.82
FeOT	3,111	0	5.98	15.3	8.05	8.01	0.675	0.569
MgO	3,111	0	31.8	50.8	43	43.6	2.96	4.38
CaO	3,111	0	0.01	5.2	1.46	1.17	1.04	1.66
Na <sub>2</sub> O	2,008	1,103	0	0.525	0.127	0.098	0.11	0.171

Note. Columns with an asterisk are in wt.%. Std, standard deviation; IQR, interquartile range.

*plutonic-ultramafic.*” The search queried 19,791 samples with rock type classifications that we did not modify from their original labels. Samples lacking analyses for SiO<sub>2</sub>, MgO, Al<sub>2</sub>O<sub>3</sub>, or CaO were excluded from the data set. All samples classified as “unknown,” chromitite, limburgite, wehrlite, undifferentiated peridotite, dunite, or pyroxenite were also excluded from the data set to focus on samples that are most likely mantellic, that is, residues of partial melting modified (or not) by refertilization, rather than products of fractional crystallization (Bowen, 1915). The data were grouped according to the remaining rock types (lherzolite and harzburgite) and outliers were removed from each group using a 1.5 interquartile range threshold applied to each chemical component. Cr and Ni measured as minor elements (ppm) were converted to Cr<sub>2</sub>O<sub>3</sub> and NiO (wt.%) and all Fe oxides were converted to Fe<sub>2</sub>O<sub>3</sub>T. Total oxides were then checked against H<sub>2</sub>O, CO<sub>2</sub>, and LOI to determine if chemical analyses were performed before or after ignition. Analyses with total oxides summing to ≤97% or ≥103% were considered erroneous, or otherwise low-quality, and excluded from the data set. All analyses were then normalized to a volatile-free basis before converting Fe<sub>2</sub>O<sub>3</sub>T to FeOT. After normalization, the final compositional space investigated includes the components Na<sub>2</sub>O-CaO-FeO-MgO-Al<sub>2</sub>O<sub>3</sub>-SiO<sub>2</sub>-TiO<sub>2</sub> (NCFMAST system). The final data set contains 3,111 chemical analyses of classified peridotite samples (Table 1).

We applied Principal Component Analysis (PCA) to the standardized peridotite data set to reduce its dimensionality from the original seven-oxides space. PCA requires complete data, so samples were first arranged by decreasing MgO and increasing SiO<sub>2</sub> content and a KN algorithm was applied to impute missing oxide analyses, which were mainly the Na<sub>2</sub>O component (see Table 1 for missing analyses counts). Following common practice, a “z-score normalization” was applied to all oxide components before running PCA. The first two principal components (PC1 and PC2) explain 78% of the variance of the data set, which we considered to be sufficient for modeling a broad range of peridotitic mantle compositions. PC1 separates samples by their TiO<sub>2</sub>, Al<sub>2</sub>O<sub>3</sub>, MgO, CaO, and Na<sub>2</sub>O contents, while PC2 separates samples by SiO<sub>2</sub> and FeO (Figure 2).

In this PC space, we drew a mixing line connecting the lherzolite and harzburgite group centroids (i.e., the median values for PC1 and PC2 for each group). The lherzolite-harzburgite mixing line was then extended until reaching the approximate location of the most fertile (Al<sub>2</sub>O<sub>3</sub>-CaO-TiO<sub>2</sub>-rich) and most refractory (MgO-rich, SiO<sub>2</sub>-poor) peridotite samples, hereafter referred to as Primitive Synthetic Upper Mantle (PSUM) and Depleted Synthetic Upper Mantle (DSUM, Figure 2b), respectively. The mixing line approximates the widest array of mantle compositions derived from the natural rock record and may be interpreted as representing the first order composition variation in response to melt extraction (depletion) or addition (refertilization) in the mantle. The mixing line therefore provides a basis for sampling synthetic bulk mantle compositions directly from PC space, which were then used to generate RocMLM training data. Similarly to the PT conditions above, the machine learning models developed here are not intended to be used for predictions outside of this compositional range and are therefore validated/tested for dry mantle compositions between PSUM and DSUM.

### 2.1.3. Reducing Bulk Mantle Compositions to a Single Fertility Index Value

Training RocMLMs with either seven oxide components or two PCs as inputs is possible. However, our targeted application (e.g., implementing RocMLMs in geodynamic codes) discourages the use of the two options because in either case it would require tracking the oxides in numerical geodynamic codes, which is currently impractical.

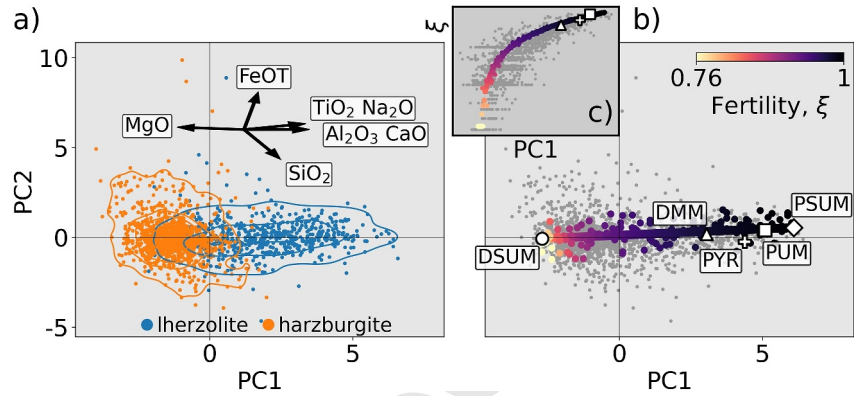


**Figure 2.** PC1–PC2 diagrams showing the standardized geochemical data set of natural peridotite samples (a) and a mixing array between hypothetical end-member mantle compositions Primitive Synthetic Upper Mantle (PSUM) and Depleted Synthetic Upper Mantle (DSUM), (b). Black arrows in (a) indicate Principal Component Analysis (PCA) loading vectors. Colored data points in (b) are the synthetic mantle compositions used to train RocMLMs, which were sampled independently from the natural peridotite samples (gray data points). The inset (c) shows how the Fertility Index ( $\xi$ ) changes nonlinearly with PC1. Depleted MORB Mantle, Primitive Upper Mantle, and PYR are from Table 2.

Thus, we aimed to reduce the dimensionality of the training data set from nine dimensions (7 oxide components + PT) to three dimensions (1 compositional dimension + PT) by estimating the amount of melt extraction (depletion) that might have produced the synthetic bulk mantle compositions in the training data set. Assuming that all synthetic samples were derived from a PSUM source, we adopt a simple modal fractional melting model (after Shaw, 1970):

$$\frac{C_{\text{TiO}_2}^x}{C_{\text{TiO}_2}^0} = R = (1 - F)^{\frac{1}{D_0} - 1} \quad (2)$$

where  $R$  is the ratio of the  $\text{TiO}_2$  concentration of the sample to the initial PSUM source (Table 2),  $F$  is the melt fraction, and  $D_0 = 0.05$  is the bulk distribution coefficient for  $\text{TiO}_2$  in peridotite (after Brown & Leshner, 2016). Note that unlike the data set of natural peridotite samples, synthetic samples were drawn directly from PC space and their  $\text{TiO}_2$  concentrations (and other oxide components) change monotonically with PC1 from the initial PSUM source (Figures 2b and 2c). Synthetic samples therefore represent a smooth and idealized variability from fertile (PSUM) to depleted (DSUM) mantle compositions that captures the average variation in natural peridotite samples.

A Fertility Index ( $\xi$ ) is calculated by rearranging Equation 2 for  $F$  and subtracting  $F$  from 1:

$$\xi = 1 - F = R^{\frac{1}{\frac{1}{D_0} - 1}} \quad (3)$$

**Table 2**  
Hypothetical Upper Mantle End-Member Compositions

Sample	SiO <sub>2</sub> *	TiO <sub>2</sub> *	Al <sub>2</sub> O <sub>3</sub> *	FeOT*	MgO*	CaO*	Na <sub>2</sub> O*	$\xi$
DSUM	44.1	0.0012	0.261	7.96	47.4	0.22	0.042	0.764
DMM	44.7	0.13	3.98	8.18	38.7	3.17	0.13	0.974
PYR	45	0.16	4.4	7.6	38.8	3.4	0.34	0.984
PUM	44.9	0.2	4.44	8.03	37.7	3.54	0.36	0.996
PSUM	46.2	0.216	4.88	8.88	35.2	4.34	0.33	1

Note. Columns with an asterisk are in wt.%. Depleted MORB Mantle (DMM) is from Workman and Hart (2005), Primitive Upper Mantle (PUM) is from Sun and McDonough (1989), and Pyrolite (PYR) is from Green (1979). Primitive Synthetic Upper Mantle (PSUM) and Depleted Synthetic Upper Mantle (DSUM), are end-member compositions derived in this study.

Training RocMLMs on  $\xi$  instead of seven oxide components is beneficial for two reasons: (a) it greatly increases RocMLM efficiency and (b) unlike oxide components or PCs, melt fraction is routinely implemented in numerical geodynamic simulations (e.g., Cerpa et al., 2019; Gerya & Yuen, 2003; Kelley et al., 2010; Li et al., 2019; Sizova et al., 2010; Yang & Facenda, 2020). Likewise, tracking the depletion/fertility of the mantle in geodynamics models with Lagrangian tracers and/or compositional fields is more conceivable (Agrusta et al., 2015; Cagnioncle et al., 2007; Gerya & Meilick, 2011; Tackley & Xie, 2003). Although we chose  $\xi$  for RocMLM training,  $\xi$  and  $F$  represent opposite reference frames for the same time-integrated melting process, and are therefore interchangeable. This approach offers a generalized solution for coupling RocMLMs to geodynamic codes.



The melting model in Equation 2 is oversimplified since it assumes: (a) melt is instantaneously removed from the source region, (b)  $D_0$  is constant, and (c) minerals melt in the same proportions that they exist in the source rock. It nevertheless provides an efficient parameterization of the variation in mantle composition as a function of melt extraction and addition. Equation 2 predicts that a Depleted MORB Mantle composition is produced through a time-integrated 2.2% melt extraction from a Primitive Upper Mantle (PUM) source (Table 2). This result is consistent with the degree of depletion inferred from trace element patterns and mass balance constraints (2%–3% melt removal from PUM, Workman & Hart, 2005). We therefore consider  $\xi$  an adequate first-order proxy for describing the variations in bulk mantle composition used in our RocMLM training data set. However, given that  $\text{TiO}_2$  concentrations are strongly affected by reactive melt transport (e.g., Le Roux et al., 2007),  $\xi$  may only be estimated for the average compositional trend as expressed in PC1-PC2 space, rather than on individual peridotite samples.

Note that the procedure above assumes a dry (i.e., volatile-free) mantle, which precludes the presence of hydrous phases and free-fluid that could significantly impact density and seismic wave velocities predicted for our training data set. Since this work was intended to demonstrate a proof-of-concept, we adopted a dry mantle assumption with the following rationale: dry mantle rocks are a simpler system to model thermodynamically with well-constrained thermodynamic data and equations of state (Stixrude & Lithgow-Bertelloni, 2022), yet provide an adequate framework for comparing RocMLM, Lookup Table, and GFEM approaches. Future works will expand the RocMLM approach to hydrous systems with a wider variety of potential mantle end-member compositions.

## 2.2. Generating RocMLM Training Data

We used the GFEM program *Perple\_X* (version 7.0.9, Connolly, 2009) to generate RocMLM training data across PT conditions as described in Section 2.1.1 and synthetic bulk mantle compositions as described in Section 2.1.2. The *Perple\_X* calculations were constrained to the  $\text{Na}_2\text{O}$ - $\text{CaO}$ - $\text{FeO}$ - $\text{MgO}$ - $\text{Al}_2\text{O}_3$ - $\text{SiO}_2$  (NCFMAS) chemical system to comply with the thermodynamic data and solution models of Stixrude and Lithgow-Bertelloni (2022). The Stixrude and Lithgow-Bertelloni (2022) data set (*stx21ver.dat*) was used because our initial tests with alternative thermodynamic data sets (*hp02ver.dat* and *hp633ver.dat*, Connolly & Kerrick, 2002; Holland & Powell, 2001; Holland et al., 2018) failed to reproduce the seismic wave velocities of geophysical reference models (PREM and STW105, Dziewoński & Anderson, 1981; Kustowski et al., 2008) with sufficient accuracy because these data sets lack a parametrization of the shear moduli of the minerals phases. Note that our *Perple\_X* calculations ignored  $\text{TiO}_2$ , which was initially included to define  $\xi$  and derive synthetic bulk mantle compositions. Despite being measured as a major oxide component, the average  $\text{TiO}_2$  content of our standardized samples is  $0.05 \pm 0.1$  wt.% ( $2\sigma$ , Table 1). Such small concentrations of  $\text{TiO}_2$  may safely be ignored in phase relation calculations with negligible effects on the RocMLM training data set.

The *Perple\_X* models used to generate the present RocMLM training database included equations of state for solution phases: olivine, plagioclase, spinel, clinopyroxene, wadsleyite, ringwoodite, perovskite, ferroperrichite, high-pressure C2/c pyroxene, orthopyroxene, akimotoite, post-perovskite, Ca-ferrite, garnet, and Na-Al phase. Melt was not considered due to the absence of melt models in the Stixrude and Lithgow-Bertelloni (2022) data set, but may be considered in future versions of training data sets if endmember shear moduli are added to the most recent thermodynamic data set that allows for mantle melting (particularly *hp633ver.dat*). Once configured, *Perple\_X* generated RocMLM training data (density, as well as P- and S-wave seismic velocities) by minimizing the total Gibbs Free Energy of a multicomponent multiphase thermodynamic system at fixed PTX conditions (Gibbs, 1878; Spear, 1993). The reader is referred to Connolly (2009) and Riel et al. (2022) for a complete description of the GFEM problem.

In principle, applying identical sets of solution phase models, thermodynamic data, and bulk compositions will define identical Gibbs Free Energy hyperplanes. This implies that any GFEM algorithm should converge on identical phase relations. Thus, although this study uses *Perple\_X* exclusively, an identical set of training data can be generated by applying the procedures outlined above to other GFEM programs. Note that RocMLM capabilities and performance are primarily dependent on the size and the range of PTX conditions of the training data set, not on the choice of GFEM algorithm.

**Table 3**  
*RocMLM Configuration*

Model	Hyperparameter	Value	Tuned
DT	Splitter	(Best, random)	Tuned
	Max features	(1, 2, 3)	Tuned
	Min samples leaf	(1, 2, 3)	Tuned
	Min samples split	(2, 4, 6)	Tuned
KN	n neighbors	(2, 4, 8)	Tuned
	Weights	(Uniform, distance)	Tuned
NN1	Hidden layer sizes	(8, 16, 32)	Tuned
NN2	Hidden layer sizes	([16, 16], [32, 16], [32, 32])	Tuned
NN3	Hidden layer sizes	([32, 16, 16], [32, 32, 16], [32, 32, 32])	Tuned
NN(all)	Learning rate	(0.001, 0.005, 0.001)	Tuned
	Batch size	20%	Fixed
	Max epochs	100	Fixed

*Note.* Hyperparameter values in parentheses are tested sequentially by a cross-validation grid search algorithm and the best set of hyperparameters is chosen by the lowest RMSE. Hyperparameters that are not shown use default values (see regression model documentation on [scikit-learn.org](https://scikit-learn.org)).

### 2.3. Training RocMLMs

RocMLM training data were preprocessed using the following procedure. First, two-dimensional grids of rock properties (“pseudosections”) calculated by *Perple\_X* were stacked into a three-dimensional array,  $Z = (z_{1,1,1}, \dots, z_{n,w,w})$ , where  $w = 128$  is the resolution of the PT grid and  $n = 128$  is the number of random synthetic bulk mantle compositions represented by a  $\xi$  value.  $Z$  was flattened into arrays of training features (PT and  $\xi$ ),  $X = (x_{1,1,1}, \dots, x_{v,v,v})$ , and training targets (density,  $V_p$ , and  $V_s$ ),  $y = (y_{1,1,1}, \dots, y_{v,v,v})$ , where  $v = n \cdot w^2 = 128^3$  is the total number of training examples. Following common practice,  $X$  and  $y$  were scaled using “z-score normalization” before training.

The preprocessed training data were then fitted with three different nonlinear regression algorithms (Decision Tree: DT, k-Neighbors: KN, and Neural Networks: NN) from the scikit-learn python library (Pedregosa et al., 2011). Each regression algorithm was tuned with a grid search approach, where a performance score (RMSE) was evaluated over all hyperparameter combinations relevant to the particular regression algorithm (Table 3). The set of hyperparameters that produced the best score (lowest RMSE) was used to train the RocMLM.

### 2.4. Evaluating RocMLM Accuracy and Performance

Connolly and Khan (2016) estimated the uncertainties of  $V_p$  and  $V_s$  to be on the order of 3%–5% within the same thermodynamic framework used to generate RocMLM training data (Stixrude & Lithgow-Bertelloni, 2005). We can therefore consider the base-uncertainty of RocMLM predictions to be 3%–5%. RocMLM predictions must also account for additional uncertainties that are introduced during RocMLM training (i.e., the variance of residuals between RocMLM predictions and targets), which are about 2% for NN1 and <1% for DT, KN, and NN3. Assuming the lowest-uncertainty models (DT, KN, NN3) would be preferred for geodynamic applications, we ignore the small variances introduced during training (<1%) and evaluate the total RocMLM prediction uncertainties to be on the same order as the base GFEM uncertainty (3%–5%) after Connolly and Khan (2016).

RocMLM accuracy (in terms of RMSE) was evaluated by: (a) the kfold cross-validation approach ( $k = 5$ ) to determine the degree to which RocMLMs can reproduce GFEM predictions (internal accuracy), and (b) comparing RocMLMs predictions with geophysical reference models PREM and STW105 (external accuracy). The kfold cross-validation approach evaluates the capability of RocMLMs to reproduce *Perple\_X* pseudosections by randomly splitting the *Perple\_X* training data into 5 folds, training RocMLMs on 4/5 folds (80% of training data), and evaluating the RMSE on the remaining fold (20% of “unseen” training data). This process is repeated for each of the 5 folds. The second test evaluates the degree to which the “true data” used for RocMLM training

(i.e., *Perple\_X* pseudosections) reproduces the phase transitions actually observed in Earth's upper mantle, which depend on the thermodynamic data, GFEM algorithm, and parameterization used to describe the composition of mantle rocks (i.e.,  $\xi$ ).

RocMLM performance was evaluated by measuring: (a) single-point prediction speeds (inference time), and (b) RocMLM model size (in Mb). Prediction speed allows us to directly compare the practicality of coupling RocMLM, GFEM, and Lookup Table approaches to high-resolution numerical geodynamic models. In contrast, model size measures the degree of information compression (or learning efficiency) for each model. For our intended purposes, prediction speed is the most practically relevant metric, because even large models ( $>10^2$ – $10^3$  Mb) are not a limiting factor for modern computer hardware.

The number of PT points and synthetic bulk mantle compositions used for generating training data were varied from 8 to 128 ( $2^{11}$ – $2^{21}$  total training examples) to test the sensitivity of RocMLM accuracy and performance with respect to the size (“capacity”) and composition of the training data set. The same sets of training data were also used to evaluate single-point prediction speed using a common Lookup Table approach, where a cubic spline interpolation was applied to the training data set and rock properties were evaluated at arbitrary PTX conditions. Prediction accuracy and performance were measured in a consistent manner so that direct comparisons could be made between RocMLMs, Lookup Tables, and GFEM programs.

### 3. Results

#### 3.1. RocMLM Accuracy

The following examples of DT (Figure 3), single-layer Neural Network (NN1, Figure 4), and three-layer Neural Network (NN3, Figure 5) models demonstrate relatively low errors (density:  $\leq 0.087$  g/cm<sup>3</sup>, Vp:  $\leq 0.271$  km/s, Vs:  $\leq 0.147$  km/s) and high correlations ( $R^2 \geq 0.93$ ) with the geophysical reference models PREM and STW105 that indicate good agreement between seismically-derived profiles and thermodynamic predictions, irrespective of regression algorithm. However, despite the general consistency between RocMLM predictions (for an average mid-ocean ridge-like geotherm) and geophysical profiles, some deviations exist, which can be partially explained by the choice of mantle geotherm, the presence (or absence) of certain phase transitions in thermodynamic versus geophysical profiles, and the choice of regression algorithm used to train RocMLMs (see Supporting Information S1 for a comparison of all regression algorithms). These effects are summarized below, leaving an explicit discussion on the effects of bulk mantle composition to Section 4.2.

DT predictions are practically indistinguishable from that of *Perple\_X*, indicating a nearly-perfect mapping of the training data set by the DT algorithm (RMSE for density: 0.006 g/cm<sup>3</sup>, Vp: 0.014 km/s, and Vs: 0.011 km/s, Figure 3). Absolute differences between *Perple\_X* and DT predictions (residuals) are broadly dispersed and approach zero in most regions of PT space. Some concentrations of residuals exist near phase transitions, but are minor and discontinuous (Figures 3g–3i). The DT algorithm therefore produces depth profiles that resolve sharp discontinuities similar to the geophysical reference models PREM and STW105 (Figures 3j–3l).

In contrast, NN1 predictions are notably smoother than *Perple\_X* (Figure 4), with higher errors (RMSE for density: 0.021 g/cm<sup>3</sup>, Vp: 0.054 km/s, Vs: 0.051 km/s) that indicate an inability to resolve sharp gradients in physical properties when using a single-layer NN with a small to moderate amount of neurons. This is evident by the NN1 residuals, which are systematically concentrated near phase transitions (Figures 4g–4i). NN1 profiles display relatively weak discontinuities with gradual changes in physical properties across the olivine  $\rightarrow$  wadsleyite and ringwoodite  $\rightarrow$  bridgmanite + ferropericlase transitions (Figures 4j–4l), and phase transformations within the MTZ are virtually absent compared to DT and NN3 profiles. However, deeper (and/or wider) NN architectures with more hidden-layers (e.g., NN3; Figure 5) are more capable and able to resolve discontinuities in geophysical profiles with nearly equivalent accuracy as DT and KN algorithms (compare profiles in Supporting Information S1).

The largest deviations between RocMLM profiles, PREM, and STW105 at pressures below the MTZ fall within two regions: (a) at  $<5$  GPa, and (b) between 5 and 8 GPa (Figures 3–5j–5l). At pressures lower than 5 GPa, the divergence between RocMLM profiles and seismically-derived profiles may be explained by the low resolution of the 1D geophysical profiles relative to the extreme spatial variability of compositions and geotherms in Earth's shallow upper mantle. For example, tests using an average continental geotherm to calculate RocMLM profiles results in less divergence between RocMLM profiles and PREM at  $<5$  GPa compared to the mid-ocean ridge-like



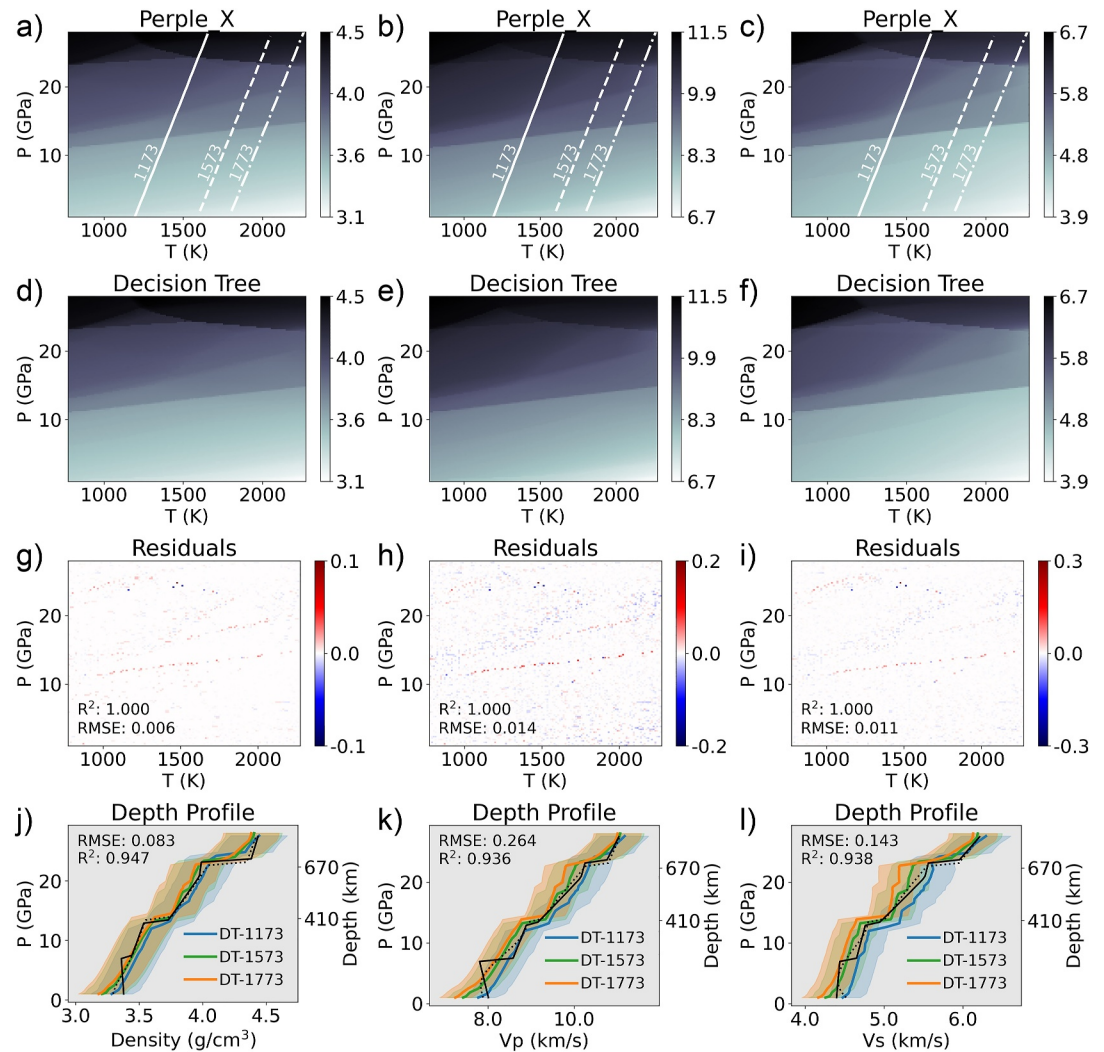


**Figure 3.** Pressure-temperature (PT) diagrams showing density (left column,  $\text{g/cm}^3$ ),  $V_p$  (middle column,  $\text{km/s}$ ), and  $V_s$  (right column,  $\text{km/s}$ ) predictions from a Perple\_X model with a Primitive Upper Mantle (PUM) bulk composition (a–c), a Decision Tree (DT) RocMLM (d–f), and absolute differences between Perple\_X and DT (g–i) measured on the training data set. Depth profiles (j–l) compare Perple\_X and DT predictions extracted along a 0.5 K/km adiabat with different mantle potential temperatures (white lines) with reference models PREM (solid black line, Dziewoński & Anderson, 1981) and STW105 (dotted black line, Kustowski et al., 2008). The RMSE in (j–l) indicates the measured differences between DT-1573 and PREM. Colored ribbons indicate 5% uncertainty in RocMLM predictions.

geotherms used to build the profiles presented in Figures 3–5. On the other hand, RocMLM profiles are more similar to STW105 between 5 and 8 GPa, which unlike PREM, does not map any discontinuities until the olivine  $\rightarrow$  wadsleyite transition at 410 km depth (Figures 3–5j–5l).

Within the MTZ, deviations between RocMLM profiles, PREM, and STW105 arise from intermediate phase transitions (e.g., wadsleyite  $\rightarrow$  ringwoodite) predicted by RocMLMs that are absent in PREM and STW105 (Figures 3 and 5g–5i). Moreover, different geotherms (i.e., mantle potential temperatures) leads to contrasting RocMLM predictions of: (a) the overall evolution of rock properties with depth, and (b) the depths, magnitudes, and sharpness of phase transitions within the MTZ (Figures 3–5g–5i). RocMLM profiles show, similarly to those directly derived from the Perple\_X calculation, temperature-sensitive discontinuities at the olivine  $\rightarrow$  wadsleyite and wadsleyite  $\rightarrow$  ringwoodite transitions, but a rather temperature insensitive ringwoodite  $\rightarrow$  bridgmanite + ferropericlasite transition (Figures 3–5g–5i). This can be explained by differences in Clapeyron slopes modeled by the Stixrude and Lithgow-Bertelloni (2022) data set.

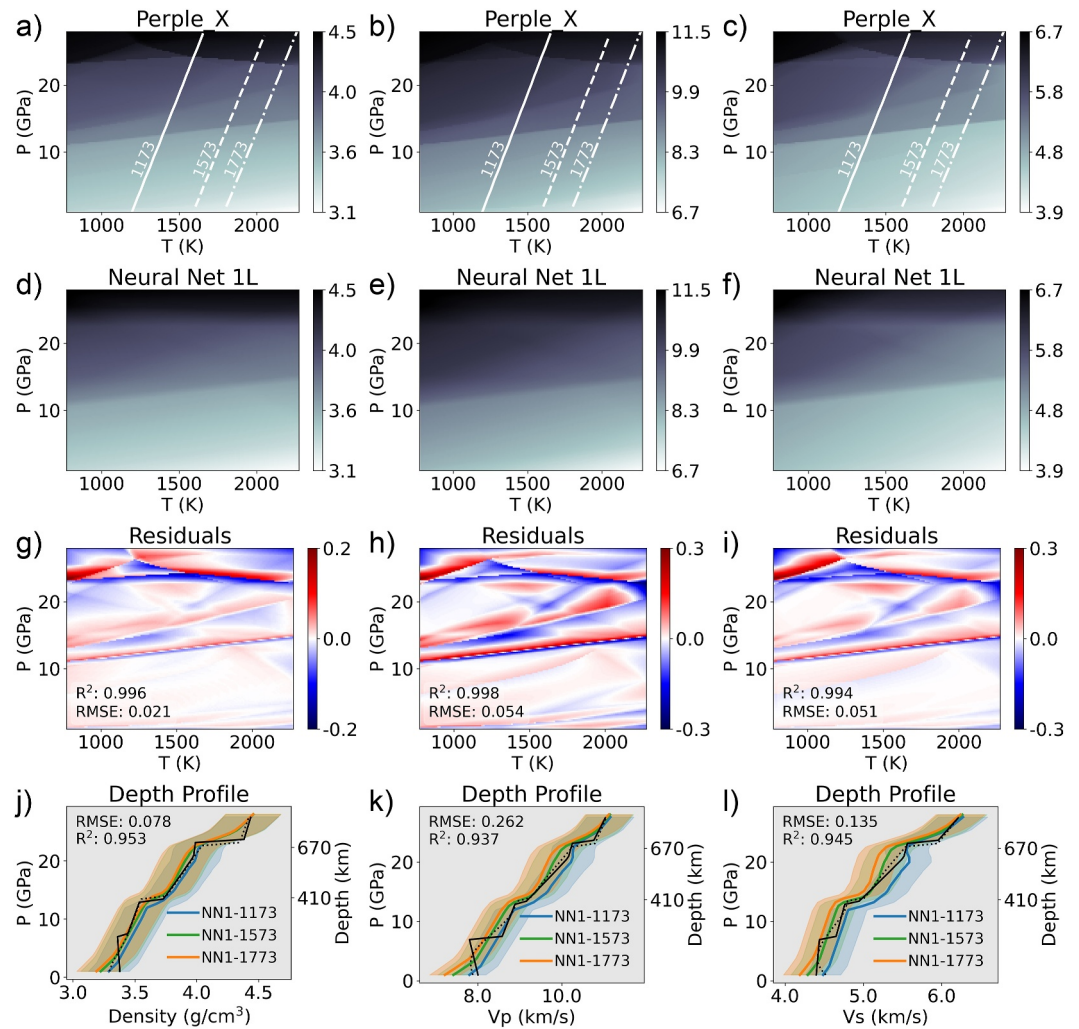


**Figure 4.** Pressure-temperature (PT) diagrams showing density (left column,  $\text{g/cm}^3$ ),  $V_p$  (middle column,  $\text{km/s}$ ), and  $V_s$  (right column,  $\text{km/s}$ ) predictions from a Perple\_X model with a Primitive Upper Mantle bulk composition (a–c), a single-layer Neural Network RocMLM (d–f), and absolute differences between Perple\_X and NN1 (g–i) measured on the training data set. Other legend details are the same as in Figure 3.

### 3.2. RocMLM Performance

We now compare RocMLM performance to two other tools classically used to predict the variations of physical properties of mantle rocks in geodynamic models: GFEM programs and Lookup Tables. Note that RocMLM, GFEM, and Lookup Table performance is platform specific. Running analogous implementations with other programming languages and/or on alternative computer hardware will differ from the results presented here. All computations in this study were made using CPUs of a Macbook Pro (2022; M2 chip) with macOS 13.4 and using Python 3.11.4. All performance metrics were evaluated with a single CPU core.

Figure 6 shows how prediction speed, size, and accuracy scale with the capacity of Lookup Tables and RocMLMs. Here, “capacity” refers to the number of scalar values stored by Lookup Tables, or alternatively, the number of pseudosection PTX points “learned” by RocMLMs. Thus, “capacity” is intended to convey and compare the breadth of petrological “knowledge,” or predictive capabilities, of Lookup Tables and RocMLMs. Within the same context, the notion of “capacity” is irrelevant for GFEM programs. Rather, GFEM performance primarily scales with the number of chemical components, phase solutions, and size of the compositional space defined by the user, as well as automatic grid refinement settings and other user-defined configuration options.

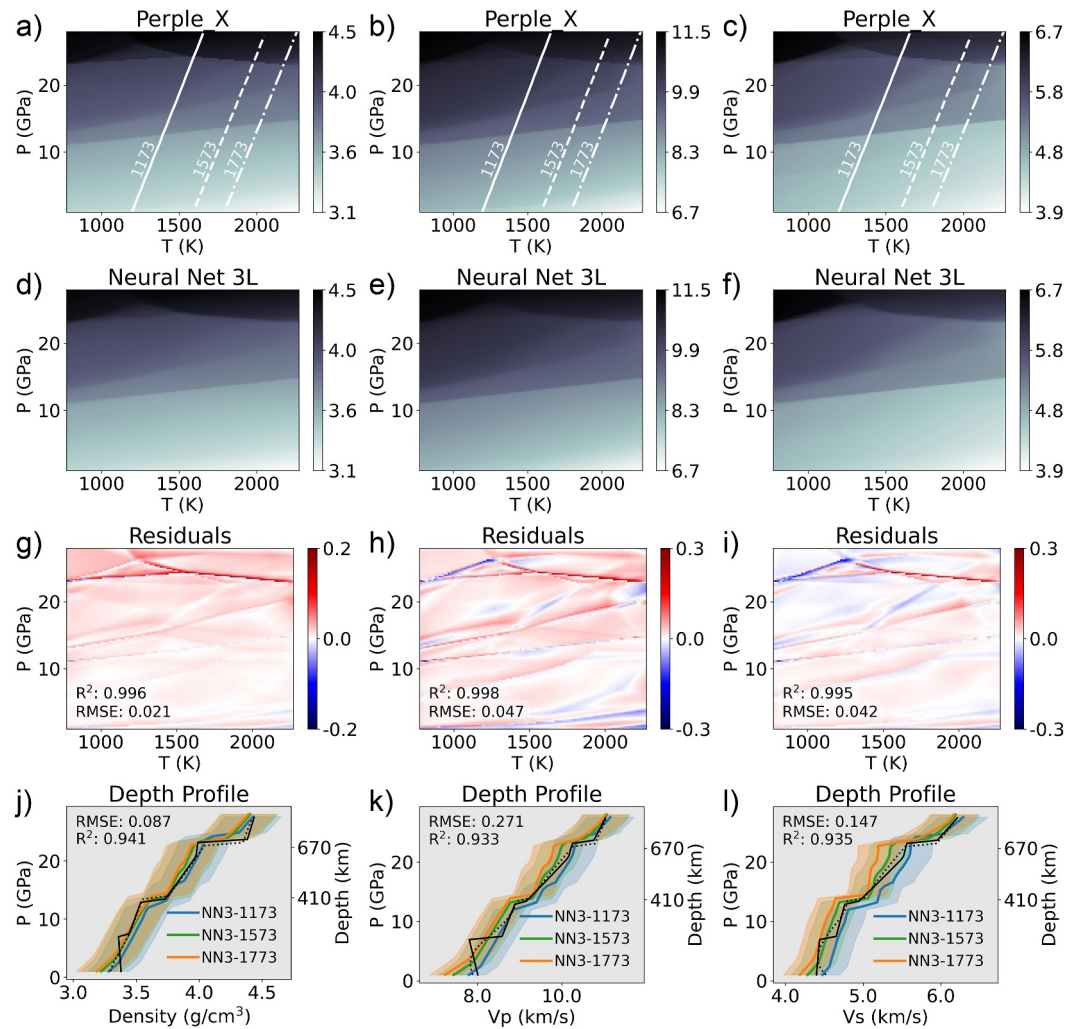


**Figure 5.** Pressure-temperature (PT) diagrams showing density (left column,  $\text{g/cm}^3$ ),  $V_p$  (middle column,  $\text{km/s}$ ), and  $V_s$  (right column,  $\text{km/s}$ ) predictions from a Perple\_X model with a Primitive Upper Mantle bulk composition (a–c), a three-layer Neural Network RocMLM (d–f), and absolute differences between Perple\_X and NN3 (g–i) measured on the training data set. Other legend details are the same as in Figure 3.

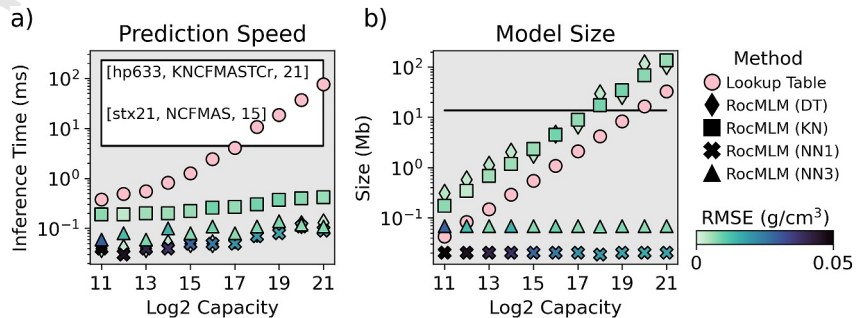


**Figure 6.** Computational efficiency of various approaches in terms of prediction speed (a) and model size (b). “Capacity” (x-axis) is a proxy for the petrological “knowledge,” or predictive capabilities, of Lookup Tables and RocMLMs. The white region in (a) indicates Gibbs Free Energy minimization (GFEM) prediction speed for different Perple\_X configurations (thermodynamic data set, chemical system, and number of solution phases are indicated in square brackets). GFEM model size is constant (bold black line). stx21: Stixrude and Lithgow-Bertelloni (2022), hp633: Holland and Powell (2011) updated in Holland et al. (2018). Perple\_X was run without multilevel grid refinement. RMSE is measured using kfold cross-validation with  $k = 5$ .

GFEM performance is reported using the range of average prediction speeds (4–228 ms) that we measured while generating our RocMLM training data sets as described in Section 2.2. To demonstrate the sensitivity of GFEM performance to alternative *Perple\_X* configurations, we also show GFEM prediction speed for similar calculations using the thermodynamic data and phase solutions of Holland et al. (2018). Note that none of the *Perple\_X* calculations using the Holland et al. (2018) configuration were used to train RocMLMs due to inaccurate seismic velocity predictions, and their performance metrics are only shown for illustrative purposes.

For Lookup Tables, prediction speed and model size both scale roughly linearly with capacity on a logarithmic scale—indicating an inverse power-law relationship between Lookup Table capacity and performance (Figure 6). RocMLM performance, in contrast, scales differently depending on the performance metric and regression algorithm. For example, RocMLM prediction speed remains roughly constant, or increasing slightly with capacity, and shows relatively small variance among all regression algorithms ( $0.12 \pm 0.20$  ms,  $2\sigma$ , Figure 6a). Yet RocMLM model size is markedly different for DT and KN algorithms compared to NN algorithms (Figure 6b). Despite the fast execution times of KN and DT algorithms (Figure 6a), their model size scales roughly linearly with capacity on a logarithmic scale—indicating an inverse power-law relationship between information compression and capacity similar to Lookup Tables (Figure 6b). NN algorithms, on the other hand, show roughly constant model size that indicate a high degree of information compression without sacrificing prediction speed (Figure 6b). We note that although directly comparing training times among RocMLMs is unfair in part due to differences in their regression algorithms and initial hyperparameters, training times for NN algorithms are many orders of magnitude larger than DT and KN algorithms (Supporting Information S1). However, training times are neither limiting nor critical for geodynamic applications as training is independent from, and precedes numerical simulations. Therefore this study focuses only on RocMLM performance after training (i.e., prediction speed), which is the most important metric when considering the practicality of coupling RocMLMs to high-resolution numerical geodynamic models.

Since accuracy is measured relative to the rock properties generated by GFEM programs, GFEM programs have perfect accuracy by definition. With respect to RocMLMs, internal accuracies (i.e., the ability to reproduce GFEM predictions) are observed to be roughly constant for regression algorithms that apply binary decisions or local distance-based weights (DT and KN), while algorithms that apply global activation-based weights (NNs) show a positive correlation between accuracy and capacity (Figure 6). In addition to improving accuracy with increasing amounts of training examples, NN accuracy also increases with the number of hidden-layers (Figure 6) because deeper networks are more capable of fitting sharp gradients in the training data (see Supporting Information S1 for examples of NN1, NN2, and NN3 RocMLMs). We also tested the effects of NN width (changing the number of nodes within each hidden layer), but this had a negligible impact on NN performance and accuracy compared to increasing NN depth.

## 4. Discussion

### 4.1. RocMLM Performance Tradeoffs

RocMLM performance and accuracy are both critical for geodynamic applications and crucial for determining if RocMLMs are an improvement over methods commonly used for predicting rock properties in numerical geodynamic simulations. In terms of pure prediction speed, our testing demonstrates that RocMLMs can make predictions between  $10^1$ – $10^3$  times faster than GFEM programs and Lookup Tables (Figure 6), depending on the GFEM program configuration. The difference in prediction speed between Lookup Tables and RocMLMs is small for low-resolution models (Figure 6) that are limited to  $\leq 16$  mantle compositions and large PT intervals ( $\geq 1.7$  GPa and 100 K PT step sizes). However, such low-resolution models are not an obvious improvement over simple polynomial approximations of a selective number of important phase transformations. At higher resolutions, RocMLMs can accurately resolve the physical properties of all thermodynamically-stable mineral assemblages in fine detail (at PT intervals of  $\leq 0.2$  GPa and 12 K) and for a wide variety of bulk mantle compositions (Figure 2). In addition to their broad predictive capabilities, high-resolution RocMLMs make predictions at speeds (approximately 0.1–1 ms, Figure 6) that allow computation of physical properties at the node-scale during geodynamic simulations. We therefore argue that high-resolution RocMLMs overcome all practical limitations for implementing thermodynamically self-consistent density evolution in numerical geodynamic models.

With respect to ranking the practicality of different RocMLM for geodynamic applications, prediction speeds and accuracies alone suggest that high-resolution RocMLMs will perform with roughly equivalent outcomes



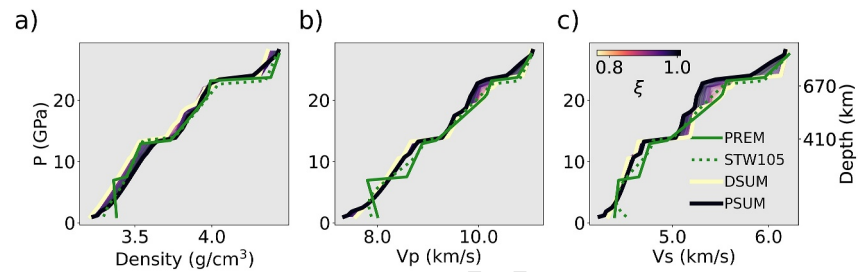


**Figure 7.** Depth profiles of RocMLM training data along a 1,573 K mantle adiabat showing the sensitivities of thermodynamic estimates of density (a),  $V_p$  (b), and  $V_s$  (c) to changes in bulk mantle composition (as represented by the Fertility Index,  $\xi$ ). Geophysical profiles PREM and STW105 (green lines) and the profiles of synthetic mantle end-member compositions Primitive Synthetic Upper Mantle and Depleted Synthetic Upper Mantle (thick colored lines) are shown for reference. Thin colored lines show profiles for the entire range of RocMLM training data.

regardless of the regression algorithm (Figure 6a). However, our testing reveals an obvious tradeoff between RocMLM performance and accuracy when accounting for compression ratio (i.e., the amount of “learned” information relative to the RocMLM file size). Figure 6b shows DT and KN algorithms becoming rapidly inefficient compared to NNs as the capacity of the training data set increases. This is because NN algorithms require relatively little information to make predictions after training (weights and biases for each neuron) compared to DT (tree structure: nodes, splits, and predictions) and KN (entire training data set with distance weights) algorithms. Moreover, accuracy tends to improve monotonically with data set capacity for NN, but not for DT or KN. We therefore argue that deep NN RocMLMs are the most practical choice for geodynamic applications for three reasons: (a) modeling more rock types only requires adding more training data, (b) adding more training data improves prediction accuracy without diminishing performance, and (c) further improvements and adaptations to different geodynamic applications are possible by exploring different architectures than the simple NN models we have tested thus far.

The main limitations of NN RocMLMs are twofold: (a) training is computationally expensive compared to other regression algorithms (Supporting Information S1) and (b) shallow NN architectures imply smoother gradients in rock properties than GFEM calculations. We do not consider these limitations critical because training time is independent from RocMLM performance and even if deeper NN architectures are needed to fit discontinuities in rock properties with high accuracy, the number of layers and neurons in each layer remains small (Table 3). We note that our testing has been limited to the prediction of three properties that are mostly P-dependent and are relatively continuous despite a few large discontinuities. In principle, RocMLMs can be trained on any thermodynamic variable output by GFEM programs. However, we have not yet trained RocMLMs on more discrete, discontinuous, and/or highly T-dependent variables, such as modal proportions of minerals, volatile contents, or melt fraction, which will be treated in future developments of RocMLMs.

#### 4.2. Geophysical and Thermodynamic Estimates of Elastic Properties

The amount of overlap between RocMLM profiles and PREM (Figures 3–3) suggests good agreement between thermodynamic and geophysical estimates of the elastic properties of mantle rocks within the limits of our training data set and Perple\_X configuration (see Sections 2.1 and 2.2). Discrepancies between thermodynamic profiles and PREM can be explained by chemical heterogeneity and/or differences in mantle geotherms that modify phase relations (Goes et al., 2022; Karki & Stixrude, 1999; Karki et al., 2001; Stixrude & Lithgow-Bertelloni, 2012; Waszek et al., 2021; Xu et al., 2008). Because the RocMLM training data set spans a wide array of synthetic bulk mantle compositions, we can directly test the sensitivity of thermodynamic estimates to changes in bulk FeO–MgO contents (Figure 7).

As Fertility Index ( $\xi$ ) increases by refertilization and/or lack of melt extraction and the bulk mantle composition becomes more Fe-rich (and more dense),  $V_p$  and  $V_s$  respond (both positively and negatively) according to the equations of state described in Stixrude and Lithgow-Bertelloni (2005). RocMLM training data show that density is the least sensitive parameter to  $\xi$  overall with only modest variations across a broad range of mantle rocks from fertile to highly depleted ( $\xi = 0.76$ , Figure 7a). The largest density variations occur at pressures below the



olivine → wadsleyite transition (<410 km), yet are still small enough (approximately 3%–5%) to imply that spontaneous mantle convection requires strong thermal gradients and/or hydration by metamorphic fluids in addition to melt extraction.

In contrast to density,  $V_p$  and  $V_s$  are more sensitive to  $\xi$  overall, especially at pressures above the olivine → wadsleyite transition (>410 km). RocMLM training data suggests that an “optimal”  $V_p/V_s$  profile requires a more depleted mantle between 410 and 670 km and a more fertile mantle at <410 km (Figures 7b and 7c). Forming this compositional layering pattern is counterintuitive, however, as partial melting is expected to be more pervasive at lower pressures. Moreover, density profiles are incongruent with this pattern, suggesting instead that a depleted mantle at <410 km and more fertile mantle at >410 km are required for an optimal fit with PREM and STW105 (Figure 7a).

## 5. Conclusions

The dynamics of Earth's upper mantle is largely driven by density contrasts stemming from changes in PT conditions, which lead to phase transformations in mantle rocks. These phase transformations also modify the elastic properties of mantle rocks. Therefore phase changes must be considered when inverting present-day mantle structure from seismic data. Likewise, numerical geodynamic simulations of mantle convection must account for thermodynamics, but are typically implemented with simple PT-dependent parameterizations of rock properties and phase boundaries that do not explicitly account for changes in Gibbs Free Energy resulting from changes in PT and in bulk composition. Here, we introduce RocMLMs as an alternative to GFEM programs and we evaluate RocMLM performance and accuracy. We also show how the RocMLM predictions compare to PREM and STW105. Our main findings are as follows:

1. RocMLMs predict density and elastic properties with high accuracy and are up to  $10^1$ – $10^3$  faster than commonly used methods. This improvement in prediction speed makes thermodynamically self-consistent mantle convection within high-resolution numerical geodynamic models practical for the first time.
2. RocMLMs trained with moderately deep (three hidden layers) NNs are more robust and efficient compared to RocMLMs trained with other regression algorithms, and are therefore the most practical models for coupling with numerical geodynamic codes.
3. RocMLM training data are sensitive to bulk mantle composition and geothermal gradients, yet show good agreement with PREM and STW105 for an average mantle geotherm.

Based on our results, we argue that moderately deep NN RocMLMs can be exceptional emulators of GFEM programs in geodynamic simulations that require computationally efficient predictions of rock properties. We have demonstrated that RocMLMs perform remarkably well for dry mantle rocks with compositions ranging from very fertile lherzolites to strongly depleted harzburgites and PT conditions ranging from 1 to 28 GPa and 773–2,273 K.

Moreover, the RocMLM approach can be used with any GFEM program and thermodynamic data set. Any improvement to the underlying thermodynamic data should further increase the accuracy of RocMLM predictions. Testing RocMLMs predictions on other thermodynamic variables of interest, including modal proportions of minerals, volatile contents, and melt fractions will be the focus of future studies. Likewise, in future works, we will extend the training data to include hydrous systems and additional end-member mantle compositions (e.g., pyroxenites and dunites).

## Data Availability Statement

All data, code, and relevant information for reproducing this work are published on GitHub (Kerswell et al., 2024a) and archived on the Open Science Framework data repository (Kerswell et al., 2024b). All code is MIT Licensed and free for use and distribution (see license details). Reference models PREM and STW105 are freely available from the Incorporated Research Institutions for Seismology Earth Model Collaboration (Trabant et al., 2012). All computations were made using CPUs of a Macbook Pro (2022; M2 chip) with macOS 14.5 and using Python 3.12.3.

### Acknowledgments

We gratefully thank Dr. Zhou Zhang and one anonymous reviewer for their thoughtful feedback that helped improve this work. We also thank Dr. Yangkang Chen and the editorial staff at JGR: MLC for their adept and efficient handling of this manuscript. This work was supported by the Tremplin-ERC Grant LEARNING awarded to Nestor Cerpa by the I-SITE excellence program at the Université de Montpellier. We thank Maurine Montagnat, Fernando Carazo, Nicolas Berlie, and many researchers and students at Géosciences Montpellier for their thoughtful feedback during the development of this work. We gratefully acknowledge additional support from the European Research Council (ERC) under the European Union Horizon 2020 Research and Innovation program Grant agreement No. 882450 (ERC RhEoVOLUTION) awarded to Andréa Tommasi.

### References

- Agrusta, R., Goes, S., & van Hunen, J. (2017). Subducting-slab transition-zone interaction: Stagnation, penetration and mode switches. *Earth and Planetary Science Letters*, 464, 10–23. <https://doi.org/10.1016/j.epsl.2017.02.005>
- Agrusta, R., Tommasi, A., Arcay, D., Gonzalez, A., & Gerya, T. (2015). How partial melting affects small-scale convection in a plume-fed sublithospheric layer beneath fast-moving plates. *Geochemistry, Geophysics, Geosystems*, 16(11), 3924–3945. <https://doi.org/10.1002/2015gc005967>
- Akaogi, M., Ito, E., & Navrotsky, A. (1989). Olivine-modified spinel-spinel transitions in the system  $Mg_2SiO_4$ - $Fe_2SiO_4$ : Calorimetric measurements, thermochemical calculation, and geophysical application. *Journal of Geophysical Research*, 94(B11), 15671–15685. <https://doi.org/10.1029/jb094ib11p15671>
- Akaogi, M., Takayama, H., Kojitani, H., Kawaji, H., & Atake, T. (2007). Low-temperature heat capacities, entropies and enthalpies of  $mg_2sio_4$  polymorphs, and  $\alpha$ - $\beta$ - $\gamma$  and post-spinel phase relations at high pressure. *Physics and Chemistry of Minerals*, 34(3), 169–183. <https://doi.org/10.1007/s00269-006-0137-3>
- Ballmer, M., Schmerr, N., Nakagawa, T., & Ritsema, J. (2015). Compositional mantle layering revealed by slab stagnation at ~1000-km depth. *Science Advances*, 1(11), e1500815. <https://doi.org/10.1126/sciadv.1500815>
- Bina, C., & Helffrich, G. (1994). Phase transition Clapeyron slopes and transition zone seismic discontinuity topography. *Journal of Geophysical Research*, 99(B8), 15853–15860. <https://doi.org/10.1029/94jb00462>
- Brown, E., & Leshner, C. (2016). REEBOX PRO: A forward model simulating melting of thermally and lithologically variable upwelling mantle. *Geochemistry, Geophysics, Geosystems*, 17(10), 3929–3968. <https://doi.org/10.1002/2016gc006579>
- Cagnioncle, A., Parmentier, E., & Elkins-Tanton, L. (2007). Effect of solid flow above a subducting slab on water distribution and melting at convergent plate boundaries. *Journal of Geophysical Research*, 112(B9), B09402. <https://doi.org/10.1029/2007jb004934>
- Cerpa, N., Arcay, D., & Padrón-Navarta, J. (2022). Sea-level stability over geological time owing to limited deep subduction of hydrated mantle. *Nature Geoscience*, 15(5), 423–428. <https://doi.org/10.1038/s41561-022-00924-3>
- Cerpa, N., Wada, I., & Wilson, C. (2019). Effects of fluid influx, fluid viscosity, and fluid density on fluid migration in the mantle wedge and their implications for hydrous melting. *Geosphere*, 15(1), 1–23. <https://doi.org/10.1130/ges011660.1>
- Christensen, U. (1995). Effects of phase transitions on mantle convection. *Annual Review of Earth and Planetary Sciences*, 23(1), 65–87. <https://doi.org/10.1146/annurev.ea.23.050195.000433>
- Čížková, H., & Bina, C. (2013). Effects of mantle and subduction-interface rheologies on slab stagnation and trench rollback. *Earth and Planetary Science Letters*, 379, 95–103. <https://doi.org/10.1016/j.epsl.2013.08.011>
- Connolly, J. (2009). The geodynamic equation of state: What and how. *Geochemistry, Geophysics, Geosystems*, 10(10), Q10014. <https://doi.org/10.1029/2009gc002540>
- Connolly, J., & Kerrick, D. (2002). Metamorphic controls on seismic velocity of subducted oceanic crust at 100–250 km depth. *Earth and Planetary Science Letters*, 204(1–2), 61–74. [https://doi.org/10.1016/s0012-821x\(02\)00957-3](https://doi.org/10.1016/s0012-821x(02)00957-3)
- Connolly, J., & Khan, A. (2016). Uncertainty of mantle geophysical properties computed from phase equilibrium models. *Geophysical Research Letters*, 43(10), 5026–5034. <https://doi.org/10.1002/2016gl068239>
- Dziewoński, A., & Anderson, D. (1981). Preliminary reference earth model. *Physics of the Earth and Planetary Interiors*, 25(4), 297–356. [https://doi.org/10.1016/0031-9201\(81\)90046-7](https://doi.org/10.1016/0031-9201(81)90046-7)
- Fukao, Y., Widiyantoro, S., & Obayashi, M. (2001). Stagnant slabs in the upper and lower mantle transition region. *Reviews of Geophysics*, 39(3), 291–323. <https://doi.org/10.1029/1999rg000068>
- Gerya, T., & Meilick, F. (2011). Geodynamic regimes of subduction under an active margin: Effects of rheological weakening by fluids and melts. *Journal of Metamorphic Geology*, 29(1), 7–31. <https://doi.org/10.1111/j.1525-1314.2010.00904.x>
- Gerya, T., & Yuen, D. (2003). Rayleigh–Taylor instabilities from hydration and melting propel ‘cold plumes’ at subduction zones. *Earth and Planetary Science Letters*, 212(1–2), 47–62. [https://doi.org/10.1016/s0012-821x\(03\)00265-6](https://doi.org/10.1016/s0012-821x(03)00265-6)
- Gibbs, J. (1878). On the equilibrium of heterogeneous substances. *American Journal of Science*, 3(96), 441–458. <https://doi.org/10.2475/ajs.s3-16.96.441>
- Goes, S., Yu, C., Ballmer, M., Yan, J., & van der Hilst, R. (2022). Compositional heterogeneity in the mantle transition zone. *Nature Reviews Earth & Environment*, 3(8), 533–550. <https://doi.org/10.1038/s43017-022-00312-w>
- Green, D. (1979). Petrogenesis of mid ocean ridge basalts. In *The Earth: Its origin, structure and evolution* (pp. 200–299).
- Hirose, K. (2002). Phase transitions in pyrolytic mantle around 670-km depth: Implications for upwelling of plumes from the lower mantle. *Journal of Geophysical Research*, 107(B4), ECV3-1–ECV3-13. <https://doi.org/10.1029/2001jb000597>
- Holland, T., Green, E., & Powell, R. (2018). Melting of peridotites through to granites: A simple thermodynamic model in the system KNCFMASHTOCr. *Journal of Petrology*, 59(5), 881–900. <https://doi.org/10.1093/ptrology/egy048>
- Holland, T., & Powell, R. (2001). Calculation of phase relations involving haplogranitic melts using an internally consistent thermodynamic dataset. *Journal of Petrology*, 42(4), 673–683. <https://doi.org/10.1093/ptrology/42.4.673>
- Holland, T., & Powell, R. (2011). An improved and extended internally consistent thermodynamic dataset for phases of petrological interest, involving a new equation of state for solids. *Journal of Metamorphic Geology*, 29(3), 333–383. <https://doi.org/10.1111/j.1525-1314.2010.00923.x>
- Ishii, T., Huang, R., Fei, H., Koemets, I., Liu, Z., Maeda, F., et al. (2018). Complete agreement of the post-spinel transition with the 660-km seismic discontinuity. *Scientific Reports*, 8(1), 6358. <https://doi.org/10.1038/s41598-018-24832-y>
- Ita, J., & Stixrude, L. (1992). Petrology, elasticity, and composition of the mantle transition zone. *Journal of Geophysical Research*, 97(B5), 6849–6866. <https://doi.org/10.1029/92jb00068>
- Ito, E. (1982). Stability relations of silicate spinels, ilmenites, and perovskite. In *High pressure research in geophysics* (pp. 405–419).
- Ito, E., Akaogi, M., Topor, L., & Navrotsky, A. (1990). Negative pressure-temperature slopes for reactions forming  $mg_sio_3$  perovskite from calorimetry. *Science*, 249(4974), 1275–1278. <https://doi.org/10.1126/science.249.4974.1275>
- Ito, E., & Katsura, T. (1989). A temperature profile of the mantle transition zone. *Geophysical Research Letters*, 16(5), 425–428. <https://doi.org/10.1029/g1016i005p00425>
- Ito, E., & Takahashi, E. (1989). Postspinel transformations in the system  $Mg_2SiO_4$ - $Fe_2SiO_4$  and some geophysical implications. *Journal of Geophysical Research*, 94(B8), 10637–10646. <https://doi.org/10.1029/jb094ib08p10637>
- Jenkins, J., Cottaar, S., White, R., & Deuss, A. (2016). Depressed mantle discontinuities beneath Iceland: Evidence of a garnet controlled 660 km discontinuity? *Earth and Planetary Science Letters*, 433, 159–168. <https://doi.org/10.1016/j.epsl.2015.10.053>

- Karato, S., Riedel, M., & Yuen, D. (2001). Rheological structure and deformation of subducted slabs in the mantle transition zone: Implications for mantle circulation and deep earthquakes. *Physics of the Earth and Planetary Interiors*, 127(1–4), 83–108. [https://doi.org/10.1016/s0031-9201\(01\)00223-0](https://doi.org/10.1016/s0031-9201(01)00223-0)
- Karki, B., & Stixrude, L. (1999). Seismic velocities of major silicate and oxide phases of the lower mantle. *Journal of Geophysical Research*, 104(B6), 13025–13033. <https://doi.org/10.1029/1999jb900069>
- Karki, B., Stixrude, L., & Wentzcovitch, R. (2001). High-pressure elastic properties of major materials of earth's mantle from first principles. *Reviews of Geophysics*, 39(4), 507–534. <https://doi.org/10.1029/2000rg000088>
- Katsura, T., & Ito, E. (1989). The system  $Mg_2SiO_4$ - $Fe_2SiO_4$  at high pressures and temperatures: Precise determination of stabilities of olivine, modified spinel, and spinel. *Journal of Geophysical Research*, 94(B11), 15663–15670. <https://doi.org/10.1029/jb094i11p15663>
- Katsura, T., Yamada, H., Shinmei, T., Kubo, A., Ono, S., Kanzaki, M., et al. (2003). Post-spinel transition in  $Mg_2SiO_4$  determined by high P–T in situ X-ray diffractometry. *Physics of the Earth and Planetary Interiors*, 136(1–2), 11–24. [https://doi.org/10.1016/s0031-9201\(03\)00019-0](https://doi.org/10.1016/s0031-9201(03)00019-0)
- Kelley, K., Plank, T., Newman, S., Stolper, E., Grove, T., Parman, S., & Hauri, E. (2010). Mantle melting as a function of water content beneath the Mariana Arc. *Journal of Petrology*, 51(8), 1711–1738. <https://doi.org/10.1093/ptrology/egg036>
- Kerswell, B., Cerpa, N., Tommasi, A., Godard, M., & Padrón-Navarta, J. (2024a). RocMLMs: Predicting rock properties through machine learning models. [Collection]. *GitHub*. Retrieved from [https://github.com/buchanankerswell/kerswell\\_et\\_al\\_rocmlm](https://github.com/buchanankerswell/kerswell_et_al_rocmlm)
- Kerswell, B., Cerpa, N., Tommasi, A., Godard, M., & Padrón-Navarta, J. (2024b). RocMLMs: Predicting rock properties through machine learning models. [Collection]. *Open Science Framework*. <https://doi.org/10.17605/OSF.IO/K23TB>
- Kerswell, B., Kohn, M., & Gerya, T. (2021). Backarc lithospheric thickness and serpentine stability control slab–mantle coupling depths in subduction zones. *Geochemistry, Geophysics, Geosystems*, 22(6), e2020GC009304. <https://doi.org/10.1029/2020gc009304>
- Kuritani, T., Xia, Q., Kimura, J., Liu, J., Shimizu, K., Ushikubo, T., et al. (2019). Buoyant hydrous mantle plume from the mantle transition zone. *Scientific Reports*, 9(1), 6549. <https://doi.org/10.1038/s41598-019-43103-y>
- Kustowski, B., Ekström, G., & Dziewoński, A. (2008). Anisotropic shear-wave velocity structure of the earth's mantle: A global model. *Journal of Geophysical Research*, 113(B6), B06306. <https://doi.org/10.1029/2007jb005169>
- Le Roux, V., Bodinier, J., Tommasi, A., Alard, O., Dautria, J., Vauchez, A., & Riches, A. (2007). The Lherz spinel lherzolite: Refertilized rather than pristine mantle. *Earth and Planetary Science Letters*, 259(3–4), 599–612. <https://doi.org/10.1016/j.epsl.2007.05.026>
- Li, Z., Gerya, T., & Connolly, J. (2019). Variability of subducting slab morphologies in the mantle transition zone: Insight from petrological-thermomechanical modeling. *Earth-Science Reviews*, 196, 102874. <https://doi.org/10.1016/j.earscirev.2019.05.018>
- Litasov, K., Ohtani, E., Sano, A., Suzuki, A., & Funakoshi, K. (2005). Wet subduction versus cold subduction. *Geophysical Research Letters*, 32(13), L13312. <https://doi.org/10.1029/2005gl022921>
- Liu, M., Yuen, D., Zhao, W., & Honda, S. (1991). Development of diapiric structures in the upper mantle due to phase transitions. *Science*, 252(5014), 1836–1839. <https://doi.org/10.1126/science.252.5014.1836>
- Maruyama, S., Liou, J., & Terabayashi, M. (1996). Blueschists and eclogites of the world and their exhumation. *International Geology Review*, 38(6), 485–594. <https://doi.org/10.1080/00206819709465347>
- Morishima, H., Kato, T., Suto, M., Ohtani, E., Urakawa, S., Utsumi, W., et al. (1994). The phase boundary between  $\alpha$ - and  $\beta$ - $Mg_2SiO_4$  determined by in situ x-ray observation. *Science*, 265(5176), 1202–1203. <https://doi.org/10.1126/science.265.5176.1202>
- Nakagawa, T., & Buffett, B. (2005). Mass transport mechanism between the upper and lower mantle in numerical simulations of thermochemical mantle convection with multicomponent phase changes. *Earth and Planetary Science Letters*, 230(1–2), 11–27. <https://doi.org/10.1016/j.epsl.2004.11.005>
- Pedregosa, F., Varoquaux, G., Gramfort, A., Michel, V., Thirion, B., Grisel, O., et al. (2011). Scikit-learn: Machine learning in Python. *Journal of Machine Learning Research*, 12, 2825–2830.
- Riel, N., Kaus, B., Green, E., & Berlie, N. (2022). MAGEMin, an efficient Gibbs energy minimizer: Application to igneous systems. *Geochemistry, Geophysics, Geosystems*, 23(7), e2022GC010427. <https://doi.org/10.1029/2022gc010427>
- Ringwood, A. (1991). Phase transformations and their bearing on the constitution and dynamics of the mantle. *Geochimica et Cosmochimica Acta*, 55(8), 2083–2110. [https://doi.org/10.1016/0016-7037\(91\)90090-r](https://doi.org/10.1016/0016-7037(91)90090-r)
- Schubert, G., Yuen, D., & Turcotte, D. (1975). Role of phase transitions in a dynamic mantle. *Geophysical Journal International*, 42(2), 705–735. <https://doi.org/10.1111/j.1365-246x.1975.tb05888.x>
- Shaw, D. (1970). Trace element fractionation during anatexis. *Geochimica et Cosmochimica Acta*, 34(2), 237–243. [https://doi.org/10.1016/0016-7037\(70\)90009-8](https://doi.org/10.1016/0016-7037(70)90009-8)
- Sizova, E., Gerya, T., Brown, M., & Perchuk, L. (2010). Subduction styles in the Precambrian: Insight from numerical experiments. *Lithos*, 116(3–4), 209–229. <https://doi.org/10.1016/j.lithos.2009.05.028>
- Spear, F. (1993). Metamorphic phase equilibria and pressure-temperature-time paths. Mineralogical Society of America Monograph, 799.
- Stixrude, L., & Lithgow-Bertelloni, C. (2005). Thermodynamics of mantle minerals-I. Physical properties. *Geophysical Journal International*, 162(2), 610–632. <https://doi.org/10.1111/j.1365-246x.2005.02642.x>
- Stixrude, L., & Lithgow-Bertelloni, C. (2012). Geophysics of chemical heterogeneity in the mantle. *Annual Review of Earth and Planetary Sciences*, 40(1), 569–595. <https://doi.org/10.1146/annurev.earth.36.031207.124244>
- Stixrude, L., & Lithgow-Bertelloni, C. (2022). Thermal expansivity, heat capacity and bulk modulus of the mantle. *Geophysical Journal International*, 228(2), 1119–1149. <https://doi.org/10.1093/gji/ggab394>
- Sun, S., & McDonough, W. (1989). Chemical and isotopic systematics of oceanic basalts: Implications for mantle composition and processes. *Geological Society, London, Special Publications*, 42(1), 313–345. <https://doi.org/10.1144/gsl.sp.1989.042.01.19>
- Syracuse, E., van Keken, P., & Abers, G. (2010). The global range of subduction zone thermal models. *Physics of the Earth and Planetary Interiors*, 183(1–2), 73–90. <https://doi.org/10.1016/j.pepi.2010.02.004>
- Tackley, P., Stevenson, D., Glatzmaier, G., & Schubert, G. (1994). Effects of multiple phase transitions in a three-dimensional spherical model of convection in earth's mantle. *Journal of Geophysical Research*, 99(B8), 15877–15901. <https://doi.org/10.1029/94jb00853>
- Tackley, P., & Xie, S. (2003). STAG3D: A code for modeling thermo-chemical multiphase convection in earth's mantle. In *Computational fluid and solid mechanics 2003* (pp. 1524–1527). Elsevier.
- Torii, Y., & Yoshioka, S. (2007). Physical conditions producing slab stagnation: Constraints of the Clapeyron slope, mantle viscosity, trench retreat, and dip angles. *Tectonophysics*, 445(3–4), 200–209. <https://doi.org/10.1016/j.tecto.2007.08.003>
- Trabant, C., Hutko, A., Bahavar, M., Karstens, R., Ahern, T., & Aster, R. (2012). Data products at the IRIS DMC: Stepping stones for research and other applications [Dataset]. *Seismological Research Letters*, 83(5), 846–854. <https://doi.org/10.17611/DP/EMC.1>
- Wang, X., Wilde, S., Li, Q., & Yang, Y. (2015). Continental flood basalts derived from the hydrous mantle transition zone. *Nature Communications*, 6(1), 7700. <https://doi.org/10.1038/ncomms8700>

- Waszek, L., Tauzin, B., Schmerr, N., Ballmer, M., & Afonso, J. (2021). A poorly mixed mantle transition zone and its thermal state inferred from seismic waves. *Nature Geoscience*, *14*(12), 949–955. <https://doi.org/10.1038/s41561-021-00850-w>
- Workman, R., & Hart, S. (2005). Major and trace element composition of the Depleted MORB Mantle (DMM). *Earth and Planetary Science Letters*, *231*(1–2), 53–72. <https://doi.org/10.1016/j.epsl.2004.12.005>
- Xu, W., Lithgow-Bertelloni, C., Stixrude, L., & Ritsema, J. (2008). The effect of bulk composition and temperature on mantle seismic structure. *Earth and Planetary Science Letters*, *275*(1–2), 70–79. <https://doi.org/10.1016/j.epsl.2008.08.012>
- Yang, J., & Faccenda, M. (2020). Intraplate volcanism originating from upwelling hydrous mantle transition zone. *Nature*, *579*(7797), 88–91. <https://doi.org/10.1038/s41586-020-2045-y>

UNCORRECTED PROOF